npj | computational materials

Article

Published in partnership with the Shanghai Institute of Ceramics of the Chinese Academy of Sciences

https://doi.org/10.1038/s41524-024-01329-z

Accurate first-principles simulation for the response of 2D chemiresistive gas sensors

Shuwei Li [1,2,3] & Liang Zhang [1,2,3] ✉

The realm of chemiresistive gas sensors has witnessed a notable surge in interest in two-dimensional (2D) materials. The advancement of high-performance 2D gas sensing materials necessitates a quantitative theoretical method capable of accurately predicting their response. In this context, we present our first-principles framework for calculating the response of 2D materials, incorporating both carrier concentration and mobility. We showcase our method by applying it to prototype NH_3 sensing on 2D MoS_2 and comparing the results with prior experiments in the literature. Our approach offers a thorough solution for carrier concentration, taking into account the electronic structure around the Fermi level. In conjunction with the mobility calculation, this enables us to provide a quantitative prediction of the response profile and limit of detection (LOD), yielding a notably improved alignment with prior experimental findings. Further analysis quantifies the contributions of carrier concentration and mobility to the overall response of 2D MoS_2 to NH_3. We identify that discrepancies in the charge-transfer-based method primarily stem from overestimating carrier concentrations. Our method opens exciting opportunities to explore carrier mobility-dominated sensing materials, facilitates efficient screening of promising gas sensing materials, and quantitative understanding of the sensing mechanism.

Utilized for the detection of specific gases, including toxic gases[1], volatile organic compounds (VOCs)[2], flammable and explosive gases[3], chemiresistive gas sensors serve as electronic devices, paramount in safeguarding human health and safety[4,5]. In particular, two-dimensional (2D) materials, such as graphene[6], transition metal dichalcogenides (TMDs)[7], phosphorene[8], and MXenes[9], have risen to prominence as potential candidates for chemiresistive gas sensors due to their high surface-to-volume ratio, tunable surface functionalities, room temperature (RT) operation condition and low cost for sensor fabrication[10–12]. Within these sensors (Fig. 1a), the detection of target gases hinges on the monitoring of shifts in their electrical resistance[13]. It is well accepted that the resistance variations stem from the impact of gas adsorption on the sensing material's carrier concentration and mobility[6,14–16]. As illustrated in Fig. 1b, the generation of response in 2D chemiresistive gas sensors involves a multitude of processes, including gas adsorption, modulation of material's carrier concentration induced by the charge transfer between gas and sensing material, and carrier mobility influenced by factors like electron-phonon and ionized impurity scattering. Nevertheless, current studies fall short of comprehensively capturing these intertwined processes or quantifying the contribution of carrier concentration and mobility to the total gas response of sensing materials. The gap in understanding the intrinsic gas sensing mechanism underscores the crucial role of accurate simulations in advancing the field of 2D chemiresistive gas sensors.

The depletion layer model was first proposed to qualitatively explain the chemiresistive mechanism for metal oxide semiconductors sensor[14]. It emphasizes that the resistance alterations of sensing materials are linked to the formation of carrier depletion or accumulation layers that triggered by the adsorption of target gases[10,17]. Building on insights from the depletion layer model, several theoretical studies employed density functional theory (DFT) to investigate the sensing behavior of chemiresistive gas sensors[18–22]. For instance, Dravid et al. calculated the charge transfer between MoS_2 and specific gases, and discovered that NH_3 and NO_2 act as electron donors and acceptors to alter the carrier concentration of MoS_2, clarifying the opposite resistance shifts of MoS_2 with different gases adsorption in experiments[7]. Based on the calculated band structures by DFT, Lei et al. found that the adsorption of NH_3 on the oxygen vacancy of MoO_3 can increase the dispersion of gap state and narrow band gap, leading to a more pronounced enhancement in its conductivity, explaining its remarkable sensitivity to

[1]Center for Combustion Energy, Tsinghua University, 100084 Beijing, China. [2]School of Vehicle and Mobility, Tsinghua University, 100084 Beijing, China. [3]State Key Laboratory of Intelligent Green Vehicle and Mobility, Tsinghua University, 100084 Beijing, China. ✉e-mail: zhangbright@tsinghua.edu.cn

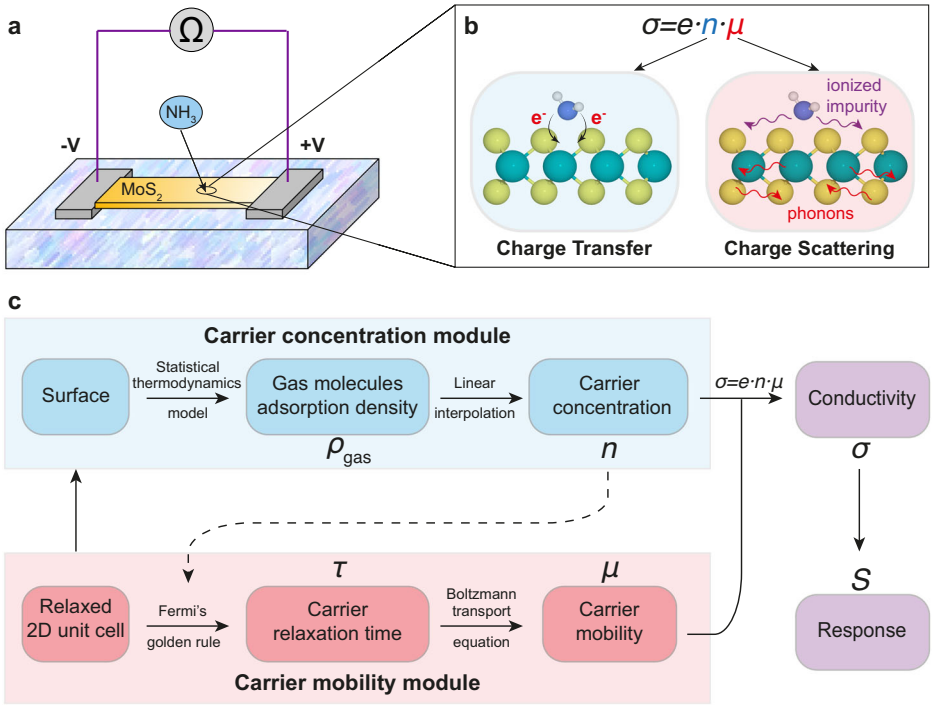

Fig. 1 | Schematics for calculating the response of 2D gas sensing materials. a Illustration of a chemiresistive gas sensor based on 2D MoS_2 for NH_3 detection. **b** Diagrammatic representation to explain the effect of gas molecules (NH_3) adsorption on the carrier concentration (left inset) and mobility (right inset) of sensing material (2D MoS_2). **c** First-principles workflow for calculating the response of 2D gas sensing materials.

NH_3[23]. Luo et al. employed the charge transfer and adsorption energy to shed light on the excellent selectivity of CdS quantum dot (QD) gel to NO_2 and the optimal combination of strong response and fast recovery achieved by PbCdSe QD gels[24,25]. Furthermore, Chen et al. introduced a charge-transfer-based approach to quantitatively access the carrier concentration of phosphorene exposed to NO_2 and successfully explained the thickness dependence[8].

However, current approaches, whether semi-quantitative or quantitative, solely based on charge transfer, leading to the following two major impediments: (1) the disregard for the impact of carrier mobility, and (2) the potential overestimation of carrier concentration changes. Moreover, the lack of a comprehensive simulation method for the full adsorption-response gas sensing process hinders the quantitative prediction of key metrics of gas sensing materials, such as response and limits of detection(LOD).

In this work, we introduce a first-principles method to calculate the response of 2D gas sensing materials, consisting of two modules: (1) a carrier concentration module, which provides more accurate carrier concentrations by considering the electronic structure around Fermi level, and (2) a carrier mobility module, which employs density functional perturbation theory (DFPT) and Wannier interpolation to compute carrier mobility that taking into account electron-phonon and ionized impurity scattering. Motivated by the abundance of experimental results of 2D MoS_2 gas sensors[7,12,26,27], we chose it as an illustrative prototype to demonstrate our computational method and its predictions. Our method can predict a reliable response that is accord with the experimental results, and give an accurate LOD. In contrast, we discover that the previous charge-transfer-based method tends to overestimate 2D MoS_2's response towards NH_3, resulting in a predicted limit of detection (LOD) that is significantly more sensitive than the experimental values by nearly 2 orders of magnitude. The analysis that decouples carrier concentration and mobility from the conductivity of MoS_2 offers a quantitative understanding of their contributions to the overall response of 2D MoS_2 to NH_3, demonstrating that its gas sensing mechanism is primarily dominated by carrier concentration, and the overestimated response or underestimated LOD in the charge-transfer-based method primarily stem from overestimating variations in carrier concentrations. Our findings not only demonstrate that the previous charge-transfer-based method offers a reasonable qualitative assessment but also reveal its limitations in providing quantitative predictions for the response of carrier concentration-dominated materials like MoS_2. Moreover, our study opens exciting opportunities for exploring materials dominated by carrier mobility like SnO_2 and alloyed $MoS_{2-x}Se_x$[15,28].

Results

First-principles framework for calculating response of 2D materials

As depicted in Fig. 1c, we start by constructing a sensing material surface from the relaxed 2D unit cell. Utilizing a statistical thermodynamics model[8,29,30], we calculate the adsorption densities ρ_{gas} of the target gas on this surface across varying gas concentrations (details in Supplementary Note 1). We then introduce a linear interpolation method to determine the corresponding carrier concentrations n of the sensing material (refer to Supplementary Note 2). Based on the computed carrier concentrations n, the carrier relaxation time τ is ascertained through Fermi's golden rule. Subsequently, the carrier mobility μ is derived from the Boltzmann transport equation (BTE), and the material's conductivity σ is obtained as $\sigma = e \cdot n \cdot \mu$. Ultimately, this enables us to gauge the response S of sensing material to various target gas concentrations (more details in Supplementary Note 3).

Carrier concentration module

To obtain the carrier concentration of 2D MoS_2 at different NH_3 concentrations, the corresponding NH_3 adsorption density on MoS_2 must first be determined. Figure 2a presents the Morse potential, represented by the black line, which is fitted using DFT results (shown as blue points). It describes the interaction between the NH_3 molecule and MoS_2 surface as a function of distance. With the fitted Morse potential, the adsorption densities of NH_3 on the bilayer MoS_2 surface upon different NH_3 concentrations are deduced through a statistical thermodynamics model (Fig. 2b, see Supplementary Note 1 for calculation details), which has been employed to calculate the adsorption density of gases on graphene[29,30] and phosphorene[8] surfaces. Subsequently, to precisely ascertain the carrier concentration of MoS_2 at arbitrary NH_3 adsorption density, we introduce a linear interpolation method (details provided in Supplementary Note 2). As illustrated in Fig. 2c, given that NH_3 acts as an electron donor, its adsorption results in an upward shift in the Fermi level of the MoS_2 surface, leading to an

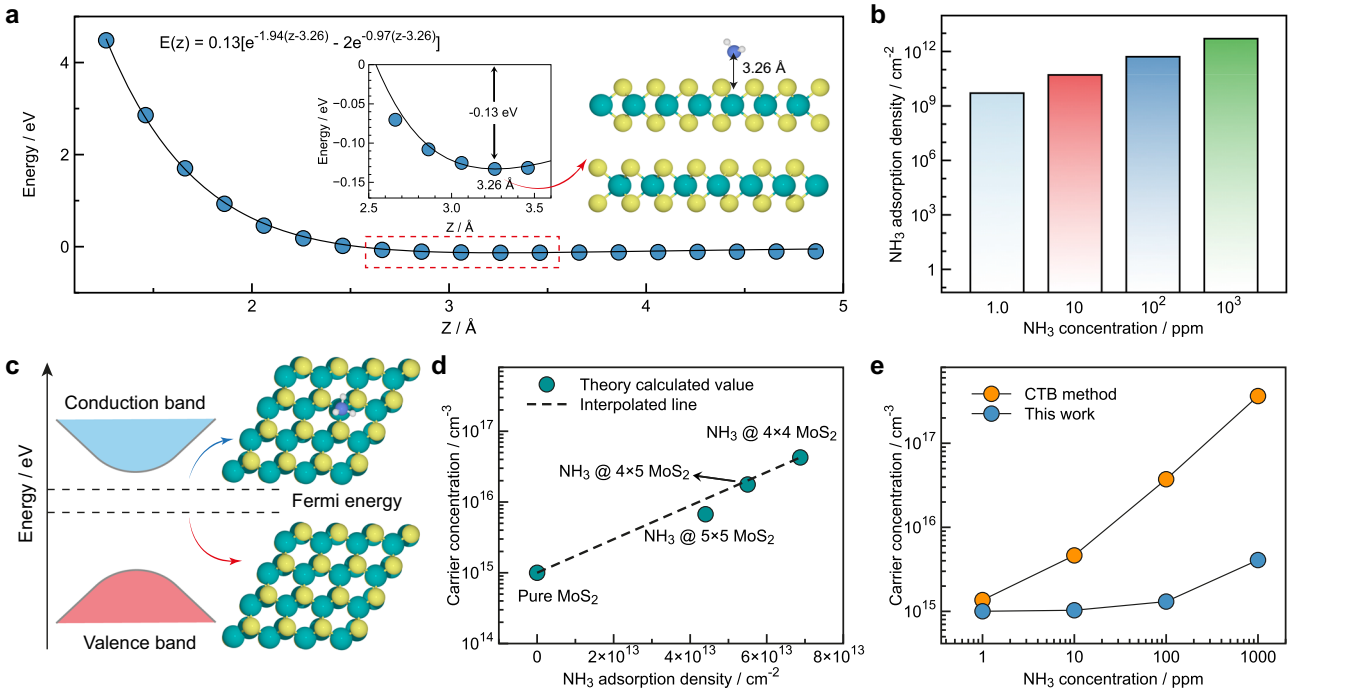

Fig. 2 | NH_3 adsorption density on bilayer MoS_2 and resultant carrier concentrations of MoS_2 under varying NH_3 concentrations. a The Morse potential type of interaction strength between the single NH_3 molecule and 4 × 4 bilayer MoS_2 surface with respect to the distance which defined as the height difference between the mass center of NH_3 and top S layer of MoS_2. The inset figure shows the most stable adsorption configuration among all possible configurations listed in Supplementary Fig. 6. The H, N, S, and Mo atoms are shown as white, blue, yellow, and green balls, respectively. **b** The NH_3 adsorption density on bilayer MoS_2 under different NH_3 concentrations. **c** The illustrative representation of the Fermi level shift induced by NH_3 adsorption on the bilayer MoS_2. **d** The comparison between the carrier concentrations calculated by theoretical method and the corresponding interpolated values. **e** The carrier concentrations of bilayer MoS_2 under different NH_3 concentrations calculated by charge-transfer-based (CTB) method (orange points, see detail in Supplementary Note 7) and our method (blue points), respectively.

increased carrier concentration. It should be pointed out that the band structure and band gap of MoS_2 surface remain largely unchanged after NH_3 adsorption, as evidenced by Supplementary Fig. 7. Moreover, the fat-band analysis (Supplementary Fig. 8) confirms that the energy bands of all atomic orbitals of NH_3 lie outside the band gap and are distant from the conduction band minimum (CBM) and valence band maximum (VBM). Consequently, the carrier concentration of the MoS_2 surface upon NH_3 adsorption can be determined based on the corresponding shift of Fermi level. However, at low NH_3 concentrations like ppm level, the adsorption density or coverage of NH_3 on the MoS_2 surface is notably low. This necessitates creating an exceptionally large MoS_2 surface, which poses a prohibitive computational burden. As indicated in Fig. 2d, the linear interpolation method offers a credible estimation for the carrier concentration of MoS_2 surface at low NH_3 concentrations. By referencing the NH_3 adsorption densities on MoS_2 surface at various NH_3 concentrations (Fig. 2b), we can determine the corresponding carrier concentrations (blue points in Fig. 2e, see detail in Supplementary Note 2). Moreover, it should be pointed out that the carrier concentrations of MoS_2 calculated by charge-transfer-based method (orange points in Fig. 2e, see detail in Supplementary Note 7) are always higher than those obtained by our method, especially noticeable at elevated NH_3 concentrations.

Carrier mobility module

For the determination of mobility, we prioritize the phonon and ionized impurity scattering in this work. Due to the extensive computational requirements of carrier mobility module (highlighted using red color in Fig. 1c), particularly those involving DFPT, we employ the bilayer MoS_2 unit cell for our carrier mobility computations. The calculated band structure in Fig. 3a demonstrates that the bilayer MoS_2 has an indirect band gap of 1.65 eV, aligning with previously reported theoretical values[31]. Figure 3b depicts the phonon dispersion of bilayer MoS_2, where the absence of imaginary frequencies confirms the dynamical stability of its structure. We also examined the band structure and phonon dispersion of monolayer MoS_2 (Supplementary Fig. 2 and Supplementary Fig. 3). Finally, the calculated carrier mobilities of monolayer and bilayer MoS_2 are 111.64 and 158.71 $cm^2 V^{-1} s^{-1}$, respectively. Notably, for the extensively studied monolayer MoS_2, our computed mobility is in good consistent with other computational values[32–34].

Furthermore, we probe into the mobility of bilayer MoS_2, which is limited by electron-phonon scattering and ionized impurity scattering across varying NH_3 concentrations. As depicted in Fig. 3c, it is evident that electron-phonon scattering is largely invariant to fluctuations in NH_3 concentrations. This finding aligns with the research conducted by Liu group[32], who utilized a more precise methodology involving quadrupole scattering to reveal the insensitivity of monolayer MoS_2 to carrier concentrations. It is widely recognized that the electron-phonon scattering is chiefly tied to lattice thermal vibrations, and has a pronounced temperature dependence[33,35–37]. In contrast, the ionized impurity scattering distinctly depends on carrier concentrations[38]. As further corroborated in Fig. 3c, the ionized impurity scattering intensifies at high carrier concentrations, which corresponds to high NH_3 concentrations, subsequently reducing the carrier mobility. Even so, the total mobility of bilayer MoS_2 remains predominantly determined by electron-phonon scattering across all NH_3 concentrations examined in this study. Figure 3d details the scattering rate, limited by electron-phonon and ionized impurity scatterings, for an electron within the conduction band spanning an energy range of 0.1 eV at 1000 ppm NH_3 concentration. This illustration confirms that the electron-phonon interaction is the primary contributor to the total scattering rate, resulting in the total mobility of 2D MoS_2 being dependent on the electron-phonon limited mobility, as demonstrated in Fig. 3c.

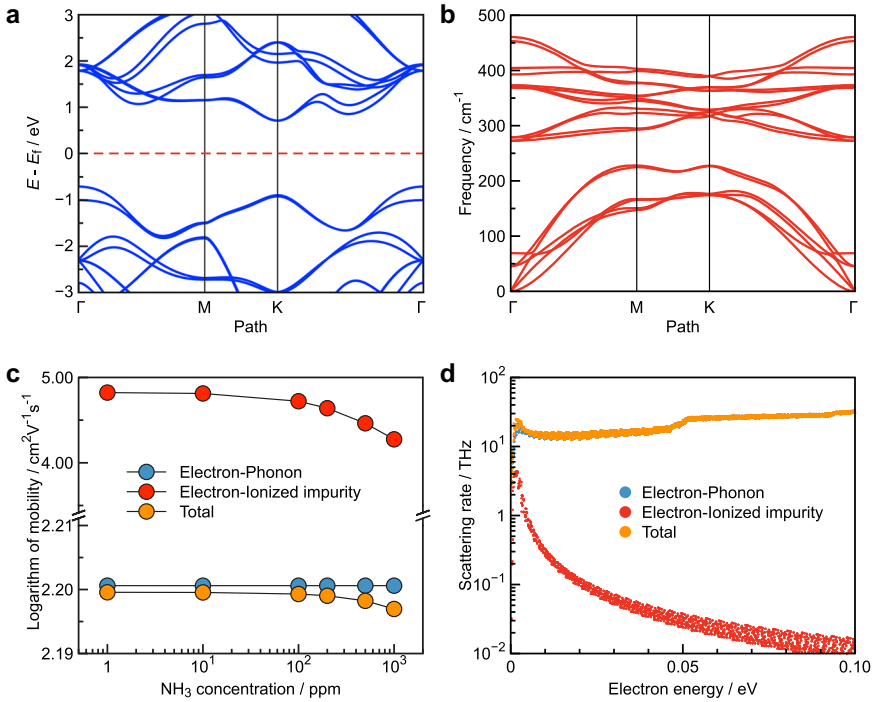

Fig. 3 | The carrier mobility and scattering rate of bilayer MoS_2 under varying NH_3 concentrations. **a** The band structure of bilayer MoS_2 unit cell. **b** The phonon dispersion of bilayer MoS_2 unit cell. **c** The logarithm of the electron–phonon limited mobility (blue points), electron-ionized impurity limited mobility (red points), and total mobility (orange points) of MoS_2 as a function of NH_3 concentrations. The total mobility can be determined by Matthiessen's rule: $\frac{1}{\mu_{total}} = \frac{1}{\mu_{e-ph}} + \frac{1}{\mu_{e-imp}}$. **d** The electron-phonon scattering rate (blue pints), electron-ionized impurity scattering rate (red points) and total scattering rate (orange points) of MoS_2 as a function of electron energy at 1000 ppm NH_3 concentration. Zero points are at the conduction band minimum. The total scattering rate (i.e. the reciprocal of relaxation time) can be determined via: $\frac{1}{\tau_{total}} = \frac{1}{\tau_{e-ph}} + \frac{1}{\tau_{e-imp}}$.

Comparison between theoretical and experimental results

Combining the carrier concentration and mobility, we derived the response of 2D MoS_2 across various NH_3 concentrations, as illustrated in Fig. 4a. Notably, the response predicted by our scheme aligns very well with experimental data[7,26]. We have also compared with the charge-transfer-based method (orange squares), using the same carrier mobility. Figure 4a shows that charge-transfer-based method tends to overestimate the response, potentially leading to an underestimated LOD. A closer look for the response of 2D MoS_2 at low NH_3 concentrations (10^{-2}–10^2 ppm) is also shown in Fig. 4b. Our results indicate a discernible response (2.75%) only starting from 10 ppm. This observation is consistent with experimental observations that pinpoint an LOD around 30 ppm for 2D MoS_2 in response to NH_3[26]. While the results of charge-transfer-based method suggest that 2D MoS_2 exhibits a detectable response (3.50%) even at 10^{-1} ppm NH_3, which is a value 2 orders of magnitude higher than both experimental results and our predictions.

To obtain a quantitative insight of carrier concentration and mobility contributions to the overall response of 2D MoS_2 to NH_3, we decouple these two factors from MoS_2's conductivity (Fig. 4c). It indicates that as NH_3 concentration rises, the conductivity of 2D MoS_2 also increases, a trend attributable to the escalating carrier concentrations. This congruence suggests that 2D MoS_2 is a carrier concentration-dominated sensing material. Specifically, at low NH_3 concentrations (<10^2 ppm), the carrier mobility of 2D MoS_2 remains relatively unchanged, indicating that the response of 2D MoS_2 to NH_3 can be reliably estimated based solely on carrier concentration. However, at higher NH_3 concentrations (>10^2 ppm), the diminishing carrier mobility tempers the conductivity growth of 2D MoS_2, resulting in a subdued response. This trade-off between carrier concentration and mobility at high NH_3 concentrations implies that the overall response of 2D MoS_2 cannot be simply determined by carrier concentration under these circumstances. These observations lead us to consider two potential culprits behind the overestimated response of the charge-transfer-based method: (1) an overestimation of the carrier concentration changes (Fig. 2e), or (2) the oversight regarding the decrease in carrier mobility (Fig. 3c). To clarify this issue, we computed the carrier concentration-based response of MoS_2, which only considers carrier concentration variations (depicted by the purple columns in Fig. 4d). It suggests that a reasonable response of 2D MoS_2 can be estimated solely from carrier concentration. Therefore, the overestimated variation in carrier concentrations ought to be the key factor that results in overestimating the response of charge-transfer-based method, not the neglecting of the decrease in carrier mobility. This overestimation arises from the fact that the calculated charges transferred from NH_3 to MoS_2 may not fully become mobile-free carriers within MoS_2. Instead, these transferred charges might either be trapped at specific sites near the interface or recombine with holes in MoS_2. Moreover, it is vital to recognize that the determination of transferred charges by different computational methods, such as Bader charge and Mulliken charge, usually manifests notable disparities[39], making the accurate prediction of carrier concentration variations by charge-transfer-based method even more challenging.

The above analysis demonstrates that charge transfer can serve as a valuable qualitative assessment of gas sensing performance, particularly for carrier concentration-dominated materials such as MoS_2. More importantly, it reveals the potential of carrier mobility engineering as a novel scheme for designing and optimizing sensing materials.

Discussion

In summary, we propose a first-principles framework to assess the gas response of 2D sensing materials, featuring two pivotal modules: (1) a carrier concentration module, designed to deliver more accurate carrier concentrations by probing the electronic structure around Fermi level, and (2) a carrier mobility module, aimed at calculating carrier mobility with DFPT and Wannier interpolation, considering electron-phonon and ionized impurity scattering. As a proof of principle, we take 2D MoS_2 as a prototype to evaluate our method. The comparative analysis with experimental results indicates that our method can provide an accurate prediction of response and LOD for 2D MoS_2 to NH_3, avoiding the overestimated response and underestimated LOD as encountered in charge-transfer-based method. Then, by decoupling carrier concentration and mobility from the conductivity of MoS_2, our analysis provides a quantitative insight into their respective contributions to the overall response of 2D MoS_2 to NH_3, demonstrating that its gas sensing mechanism is primarily dominated by carrier concentration. Finally, we find that the overestimated response or underestimated LOD in charge-transfer-based method are attributed to overestimating the changes in carrier concentrations of MoS_2 induced by

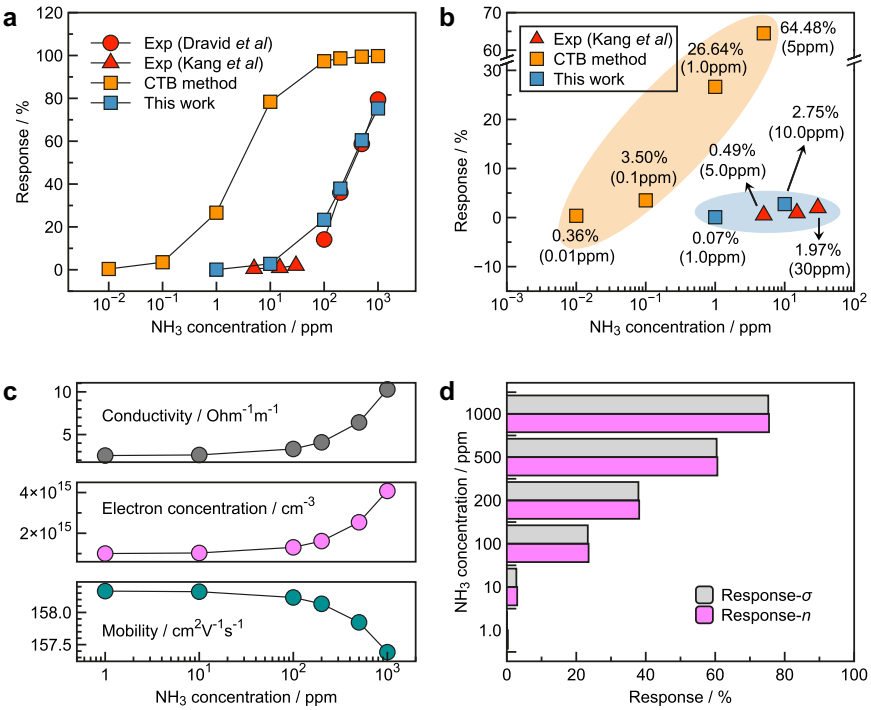

Fig. 4 | The comparison between experimental results and computational predictions. a The response of MoS_2 to different NH_3 concentrations obtained by experiments[7,26] (red points), charge-transfer-based (CTB) method (orange points, see detail in Supplementary Note 7) and our method illustrated in this work (blue points). **b** The comparison of LOD between measured in experiments (red points), predicted by charge-transfer-based method (orange points) and our method (blue points). **c** The conductivity (gray points), electron concentration (purple points), and mobility (cyan points) of MoS_2 to different NH_3 concentrations. **d** The comparison between the response (S) calculated by conductivity (gray columns, $S = \frac{|\frac{1}{\sigma_0} - \frac{1}{\sigma_{NH_3}}|}{\frac{1}{\sigma_0}} \times 100\%$) and electron concentration (purple columns, $S = \frac{|\frac{1}{n_0} - \frac{1}{n_{NH_3}}|}{\frac{1}{n_0}} \times 100\%$), respectively. σ_0 and n_0 are the conductivity and carrier concentration of pure MoS_2, respectively. σ_{NH_3} and n_{NH_3} are the conductivity and carrier concentration of MoS_2 with NH_3 adsorption, respectively.

NH_3 adsorption. Our method not only confirms the charge-transfer-based method can provide a reasonable qualitative prediction for the gas response of carrier concentration-dominated materials like MoS_2, but also opens exciting opportunities to explore carrier mobility-dominated materials such as SnO_2 and alloyed $MoS_{2-x}Se_x$[15,28]. Therefore, the first-principles method presented in this work enables us to directly screen the promising 2D materials with high gas sensing performance, and also provides a deeper understanding of their sensing mechanism, thereby paving a critical step toward the development of 2D gas sensing materials.

Methods

First-principles calculations of unit cell

All first-principles calculations are performed via the Quantum ESPRESSO package[40] with the Norm-conserving pseudopotentials and the Perdew-Burke-Ernzerhof[41] (PBE) exchange-correlation functional. A cutoff energy of 60 Ry and a $36 \times 36 \times 1$ **k**-mesh[42] are used to determine the equilibrium lattice constant until the force on each atom becomes less than 0.0001 Ry/Bohr. It has been reported that the analytic expression for Fröhlich electron-phonon matrix elements is strictly valid only in the long-wavelength limit ($\mathbf{q} \to 0$)[37,43]. To address this point, the equilibrium properties of phonons and the electron-phonon interaction matrices are calculated by density functional perturbation theory[44] for a corse $12 \times 12 \times 2$ **k**-mesh and a $12 \times 12 \times 2$ **q**-mesh. We then use the EPW software package[45] to interpolate the electronic information and phonon information, as well as the electron-phonon coupling matrices to a fine mesh using the Wannier interpolation method[46]. Based on the fat-band analysis (Supplementary Fig. 4 and Supplementary Fig. 5), the 5 *d* orbitals of Mo atom and 3 *p* orbitals of S atom are chosen as the initial guess to obtain the maximally localized Wannier Functions (MLWFs). Moreover, we compare the electronic band structures of monolayer MoS_2 using first-principles calculations and Wannier interpolation (Supplementary Fig. 9). Additionally, the similar comparison for the phonon dispersion of monolayer MoS_2 is presented in Supplementary Fig. 10. The good agreement and low spread of Wannier Functions (Supplementary Table 1 and Supplementary Table 2) ensure the reliability of our calculation. Our test results show that the calculation on a $600 \times 600 \times 4$ **k**-mesh associated with a $100 \times 100 \times 4$ **q**-mesh achieves the best balance between mobility convergence and computational efficiency for monolayer MoS_2 (Supplementary Fig. 1). Additionally, both Li et al.[47] and Late et al.[7] found that multilayer MoS_2 displays enhanced stability and sensitivity to target gases over its monolayer counterpart. We thus use this optimized mesh to compute the transport properties of bilayer MoS_2 in this work. We have included semi-empirical dispersive van der Waals (vdW) interaction using Grimme-D3 parametrization[48], which gives the closest interlayer distance (0.696 nm) of bilayer MoS_2 to experimental results (0.70 nm)[49].

First-principles calculations of slab

For calculating the adsorption density of NH_3 on the bilayer MoS_2 surface, we build a large MoS_2 slab using a bilayer 4×4 supercell of MoS_2, to avoid the interaction between adsorbed NH_3 molecules (the distance between adsorbed NH_3 molecules is larger than 10 Å). A cutoff energy of 30 Ry and a $3 \times 3 \times 1$ **k**-mesh are used to relax the system until the force on each atom becomes less than 0.0005 Ry/Bohr.

Data availability

The detailed descriptions of the method are included in the Supplementary Information (Supplementary Notes 1–7). The source data supporting the findings of this study are available via GitHub at https://github.com/ZhangLabTHU/2D-chemiresistive-gas-sensors-simulation.

Code availability

The Quantum ESPRESSO code is freely available and used on its website: https://www.quantum-espresso.org/. The EPW code can also be obtained and used freely on its website: https://epw-code.org/. The calculation of electron scattering rates through first-principles electron transport calculation in this paper is achieved via the modified EPW code developed by Zhou et al. at MIT, and is available at https://doi.org/10.24435/materialscloud:5a-7s.

Received: 17 February 2024; Accepted: 14 June 2024;
Published online: 29 June 2024

References

1. Ning, Z. et al. Air-stable n-type colloidal quantum dot solids. *Nat. Mater.* **13**, 822–828 (2014).

2. Chen, W. Y., Jiang, X., Lai, S.-N., Peroulis, D. & Stanciu, L. Nanohybrids of a MXene and transition metal dichalcogenide for selective detection of volatile organic compounds. *Nat. Commun.* **11**, 1302 (2020).
3. Favier, F., Walter, E. C., Zach, M. P., Benter, T. & Penner, R. M. Hydrogen sensors and switches from electrodeposited palladium mesowire arrays. *Science* **293**, 2227–2231 (2001).
4. Koo, W.-T., Jang, J.-S. & Kim, I.-D. Metal-organic frameworks for chemiresistive sensors. *Chem* **5**, 1938–1963 (2019).
5. Majhi, S. M., Mirzaei, A., Kim, H. W., Kim, S. S. & Kim, T. W. Recent advances in energy-saving chemiresistive gas sensors: a review. *Nano Energy* **79**, 105369 (2021).
6. Schedin, F. et al. Detection of individual gas molecules adsorbed on graphene. *Nat. Mater.* **6**, 652–655 (2007).
7. Late, D. J. et al. Sensing behavior of atomically thin-layered MoS_2 transistors. *ACS Nano* **7**, 4879–4891 (2013).
8. Cui, S. et al. Ultrahigh sensitivity and layer-dependent sensing performance of phosphorene-based gas sensors. *Nat. Commun.* **6**, 8632 (2015).
9. Kim, S. J. et al. Metallic $Ti_3C_2T_x$ MXene gas sensors with ultrahigh signal-to-noise ratio. *ACS Nano* **12**, 986–993 (2018).
10. Yang, S., Jiang, C. & Wei, S.-H. Gas sensing in 2D materials. *Appl. Phys. Rev.* **4**, 021304 (2017).
11. Cao, J. et al. Recent development of gas sensing platforms based on 2D atomic crystals. *Research* **2021**, 9863038 (2021).
12. Agrawal, A. V., Kumar, N. & Kumar, M. Strategy and future prospects to develop room-temperature-recoverable NO_2 gas sensor based on two-dimensional molybdenum disulfide. *Nano-Micro Lett.* **13**, 38 (2021).
13. Neri, G. First fifty years of chemoresistive gas sensors. *Chemosensors* **3**, 1–20 (2015).
14. Morrison, S. R. Mechanism of semiconductor gas sensor operation. *Sens. Actuators* **11**, 283–287 (1987).
15. Xu, S., Zhao, H., Xu, Y., Xu, R. & Lei, Y. Carrier mobility-dominated gas sensing: a room-temperature gas-sensing mode for SnO_2 nanorod array sensors. *ACS Appl. Mater. Interfaces* **10**, 13895–13902 (2018).
16. Li, H., Han, X., Childress, A. S., Rao, A. M. & Koley, G. Investigation of carrier density and mobility variations in graphene caused by surface adsorbates. *Physica E* **107**, 96–100 (2019).
17. Cho, B. et al. Charge-transfer-based gas sensing using atomic-layer MoS_2. *Sci. Rep.* **5**, 8052 (2015).
18. Zhao, Z., Yong, Y., Zhou, Q., Kuang, Y. & Li, X. Gas-sensing properties of the SiC monolayer and bilayer: a density functional theory study. *ACS Omega* **5**, 12364–12373 (2020).
19. Kumar, V. & Jung, J. Enhancement of gas sensing by doping of transition metal in two-dimensional As_2C_3 nanosheet: a density functional theory investigation. *Appl. Surf. Sci.* **599**, 153941 (2022).
20. Wu, Y. et al. Highly sensitive and selective gas sensor using heteroatom doping graphdiyne: a DFT study. *Adv. Electron. Mater.* **7**, 2001244 (2021).
21. Tang, X., Du, A. & Kou, L. Gas sensing and capturing based on two-dimensional layered materials: overview from theoretical perspective. *WIREs Comput. Mol. Sci.* **8**, e1361 (2018).
22. Yue, Q., Shao, Z., Chang, S. & Li, J. Adsorption of gas molecules on monolayer MoS_2 and effect of applied electric field. *Nanoscale Res. Lett.* **8**, 425 (2013).
23. Kwak, D. et al. Molybdenum trioxide (α-MoO_3) nanoribbons for ultrasensitive ammonia (NH_3) gas detection: integrated experimental and density functional theory simulation studies. *ACS Appl. Mater. Interfaces* **11**, 10697–10706 (2019).
24. Hewa-Rahinduwage, C. C. et al. Reversible electrochemical gelation of metal chalcogenide quantum dots. *J. Am. Chem. Soc.* **142**, 12207–12215 (2020).
25. Geng, X. et al. Atomically dispersed Pb ionic sites in PbCdSe quantum dot gels enhance room-temperature NO_2 sensing. *Nat. Commun.* **12**, 4895 (2021).
26. Park, J., Mun, J., Shin, J.-S. & Kang, S.-W. Highly sensitive two-dimensional MoS_2 gas sensor decorated with Pt nanoparticles. *R. Soc. Open Sci.* **5**, 181462 (2018).
27. Kumar, R., Zheng, W., Liu, X., Zhang, J. & Kumar, M. MoS_2-based nanomaterials for room-temperature gas sensors. *Adv. Mater. Technol.* **5**, 1901062 (2020).
28. Yin, M. et al. Ternary alloyed $MoS_{2-x}Se_x$ nanocomposites with a carrier mobility-dominated gas sensing mode: a superior room temperature gas sensing material for NO_2 sensors. *J. Mater. Chem. C* **11**, 9715–9726 (2023).
29. Pu, H. et al. A statistical thermodynamics model for monolayer gas adsorption on graphene-based materials: implications for gas sensing applications. *RSC Adv.* **4**, 47481–47487 (2014).
30. Lin, X., Ni, J. & Fang, C. Adsorption capacity of H_2O, NH_3, CO, and NO_2 on the pristine graphene. *J. Appl. Phys.* **113**, 034306 (2013).
31. Cheiwchanchamnangij, T. & Lambrecht, W. R. L. Quasiparticle band structure calculation of monolayer, bilayer, and bulk MoS_2. *Phys. Rev. B* **85**, 205302 (2012).
32. Zhang, C. & Liu, Y. Phonon-limited transport of two-dimensional semiconductors: quadrupole scattering and free carrier screening. *Phys. Rev. B* **106**, 115423 (2022).
33. Poncé, S., Royo, M., Stengel, M., Marzari, N. & Gibertini, M. Long-range electrostatic contribution to electron-phonon couplings and mobilities of two-dimensional and bulk materials. *Phys. Rev. B* **107**, 155424 (2023).
34. Zhou, J.-J. et al. Perturbo: A software package for ab initio electron–phonon interactions, charge transport and ultrafast dynamics. *Comput. Phys. Commun.* **264**, 107970 (2021).
35. Macheda, F., Poncé, S., Giustino, F. & Bonini, N. Theory and computation of Hall scattering factor in graphene. *Nano Lett.* **20**, 8861–8865 (2020).
36. Poncé, S., Royo, M., Gibertini, M., Marzari, N. & Stengel, M. Accurate prediction of Hall mobilities in two-dimensional materials through gauge-covariant quadrupolar contributions. *Phys. Rev. Lett.* **130**, 166301 (2023).
37. Li, W., Poncé, S. & Giustino, F. Dimensional crossover in the carrier mobility of two-dimensional semiconductors: the case of InSe. *Nano Lett.* **19**, 1774–1781 (2019).
38. Leveillee, J., Zhang, X., Kioupakis, E. & Giustino, F. Ab initio calculation of carrier mobility in semiconductors including ionized-impurity scattering. *Phys. Rev. B* **107**, 125207 (2023).
39. Guerra, C. F., Handgraaf, J.-W., Baerends, E. J. & Bickelhaupt, F. M. Voronoi deformation density (vdd) charges: assessment of the mulliken, bader, hirshfeld, weinhold, and vdd methods for charge analysis. *J. Comput. Chem.* **25**, 189–210 (2004).
40. Giannozzi, P. et al. QUANTUM ESPRESSO: a modular and open-source software project for quantum simulations of materials. *J. Phys. Condens. Matter* **21**, 395502 (2009).
41. Perdew, J. P., Burke, K. & Ernzerhof, M. Generalized gradient approximation made simple. *Phys. Rev. Lett.* **77**, 3865–3868 (1996).
42. Monkhorst, H. J. & Pack, J. D. Special points for Brillouin-zone integrations. *Phys. Rev. B* **13**, 5188–5192 (1976).
43. Verdi, C. & Giustino, F. Fröhlich electron-phonon vertex from first principles. *Phys. Rev. Lett.* **115**, 176401 (2015).
44. Baroni, S., de Gironcoli, S., Dal Corso, A. & Giannozzi, P. Phonons and related crystal properties from density-functional perturbation theory. *Rev. Mod. Phys.* **73**, 515–562 (2001).
45. Poncé, S., Margine, E. R., Verdi, C. & Giustino, F. EPW: electron–phonon coupling, transport and superconducting properties using maximally localized Wannier functions. *Comput. Phys. Commun.* **209**, 116–133 (2016).
46. Mostofi, A. A. et al. wannier90: a tool for obtaining maximally-localised Wannier functions. *Comput. Phys. Commun.* **178**, 685–699 (2008).
47. Li, H. et al. Fabrication of single-and multilayer MoS_2 film-based field-effect transistors for sensing NO at room temperature. *Small* **8**, 63–67 (2012).

48. Grimme, S., Antony, J., Ehrlich, S. & Krieg, H. A consistent and accurate ab initio parametrization of density functional dispersion correction (DFT-D) for the 94 elements H-Pu. *J. Chem. Phys.* **132**, 154104 (2010).
49. Wu, S. et al. Electrical tuning of valley magnetic moment through symmetry control in bilayer MoS_2. *Nat. Phys.* **9**, 149–153 (2013).

Acknowledgements

This work was supported by the National Natural Science Foundation of China (22373055), State Key Laboratory of Intelligent Green Vehicle and Mobility under Project No. ZZ2023-063, Tsinghua University Initiative Scientific Research Program and Center of High Performance Computing. We thank Prof. Long Luo at Wayne State University and Prof. Yuanyue Liu at the University of Texas at Austin for their helpful discussions; Dr. Xianqing Lin at the Zhejiang University of Technology and Dr. Haihun Pu at the University of Chicago for their helpful discussions on the statistical thermodynamics model; Dr. Jiawei Zhou at MIT for his helpful discussions on the calculation of electron scattering rates through first-principles electron transport calculation.

Author contributions

S.L. Conceptualization, Methodology, Visualization, Data curation, Writing-original draft. L.Z. Conceptualization, Methodology, Supervision, Resources, Writing-review & editing.

Competing interests

The authors declare no competing interests.

Additional information

Supplementary information The online version contains supplementary material available at https://doi.org/10.1038/s41524-024-01329-z.

Correspondence and requests for materials should be addressed to Liang Zhang.